

SARe: Structure-Aware Large-Scale 3D Fragment Reassembly

Hanze Jia¹, Chunshi Wang², Yuxiao Yang¹, Zhonghua Jiang¹, Yawei Luo², Shuainan Ye¹, and Tan Tang³

¹ State Key Lab of CAD&CG, Zhejiang University
{hzjia,yuxiaoyang,jiangzhonghua,snye}@zju.edu.cn

² School of Software Technology, Zhejiang University
{chunshiwang,yaweiluo}@zju.edu.cn

³ Laboratory of Art and Archaeology Image, Zhejiang University
tangtan@zju.edu.cn

Abstract. 3D fragment reassembly aims to recover the rigid poses of unordered fragment point clouds or meshes in a common object coordinate system to reconstruct the complete shape. The problem becomes particularly challenging as the number of fragments grows, since the target shape is unknown and fragments provide weak semantic cues. Existing end-to-end approaches are prone to cascading failures due to unreliable contact reasoning, most notably inaccurate fragment adjacencies. To address this, we propose **Structure-Aware Reassembly (SARe)**, a generative framework with **SARe-Gen** for Euclidean-space assembly generation and **SARe-Refine** for inference-time refinement, with explicit contact modeling. SARe-Gen jointly predicts fracture-surface token probabilities and an inter-fragment contact graph to localize contact regions and infer candidate adjacencies. It adopts a query-point-based conditioning scheme and extracts aligned local geometric tokens at query locations from a frozen geometry encoder, yielding queryable structural representations without additional structural pretraining. We further introduce an inference-time refinement stage, SARe-Refine. By verifying candidate contact edges with geometric-consistency checks, it selects reliable substructures and resamples the remaining uncertain regions while keeping verified parts fixed, leading to more stable and consistent assemblies in the many-fragment regime. We evaluate SARe across three settings, including synthetic fractures, simulated fractures from scanned real objects, and real physically fractured scans. The results demonstrate state-of-the-art performance, with more graceful degradation and higher success rates as the fragment count increases in challenging large-scale reassembly.

Keywords: Point Cloud Registration · Rectified Flow · Multi-Part Assembly

1 Introduction

3D fragment reassembly is a fundamental problem in applications such as digital heritage restoration, robotic assembly, and accident scene reconstruction [1, 7,

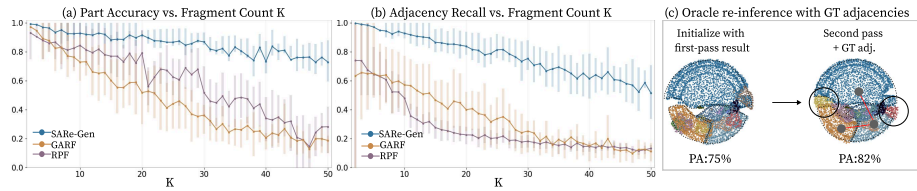


Fig. 1: As the fragment count K increases, (a) part accuracy drops and (b) adjacency recall of the induced contact graph decreases accordingly, indicating growing contact-structure errors at larger scales. (c) As an oracle diagnostic, re-inference of RPF conditioned on a small set of GT adjacencies improves an example assembly. All results are computed on the Breaking Bad dataset.

14, 38, 57]. Given a set of fragment point clouds or meshes from the object, the objective is to recover the rigid-body pose of each fragment in a common object coordinate system to restore the complete shape. Importantly, a valid reconstruction is more than a collection of poses; it also induces a contact structure. This structure specifies *where* contacts occur on fracture surfaces and *which* fragments are adjacent, jointly constraining a globally consistent reassembly. This problem remains highly challenging because the target shape is unknown, while fragments are typically irregular with few semantic cues [26, 41].

Early methods relied on explicit geometric matching and global optimization, yielding reasonable results under regular fracture patterns or with a small number of fragments [6, 10]. Spurred by the advent of large-scale 3D fracture datasets [36], learning-based approaches have advanced from geometric matching to end-to-end pose regression, directly predicting per-fragment rigid transformations from fragment geometry [11, 27, 33, 43]. More recently, diffusion-based generative frameworks have been brought to this task. Given fragment point clouds as input, diffusion-based methods either denoise pose variables to directly generate per-fragment $SE(3)$ transformations [18, 20, 25, 42, 47], or denoise point coordinates in a shared reference frame and then recover poses [39], thereby achieving state-of-the-art performance on standard benchmarks.

However, as the fragment count increases, existing methods struggle to scale robustly, and assembly performance drops significantly. As shown in Fig. 1, we further find that this drop goes hand in hand with contact-structure errors. In the contact adjacency graph computed from the predicted assemblies, the adjacency recall consistently decreases as the fragment count grows.⁴ Moreover, as an oracle diagnostic, we find that conditioning a second inference on a small subset of ground-truth adjacencies can improve the assembly quality (Fig. 1-c). This diagnostic suggests that the scalability bottleneck lies not only in pose estimation but also in the growing uncertainty of inter-fragment contact relations at large fragment counts. Once key adjacencies are misidentified, errors can propagate and amplify through the global assembly, leading to cascading

⁴ RPF [39] and GARF [20] do not output adjacency graphs. For these methods, adjacency recall is computed by inducing a contact graph from the predicted assembly.

failures. Existing methods often treat inter-fragment adjacency as an implicit signal [18, 20, 25, 39, 42, 47]; even when an adjacency matrix is explicitly predicted or inferred post hoc from contacts, it is rarely used as an actionable structural object to steer inference-time correction [33, 47]. Meanwhile, the inference process often lacks a closed-loop procedure that feeds back the current assembly and fixes adjacency errors. Once adjacency relations drift, structural errors become difficult to correct. In real-world settings, where fragments are often hard to distinguish semantically and are numerous, such structural uncertainty is further amplified and can trigger cascading failures. Therefore, successful reassembly demands both accurate pose estimation and explicit structural cues, where reliable adjacency prediction serves as an actionable constraint for global consistency.

Motivated by this, we propose **Structure-Aware Reassembly (SARe)**, a structure-aware generative framework that couples assembly generation with contact reasoning. **SARe-Gen** produces high-quality assemblies in Euclidean space while modeling how fragments should contact each other. When needed, we further apply **SARe-Refine**, which uses the predicted contact structure to anchor reliable adjacencies and resample uncertain regions, improving robustness in the many-fragment regime.

Specifically, unlike approaches that directly regress fragment poses in $SE(3)$, and inspired by 3D point cloud generation methods [16, 55] as well as point level diffusion models [39], SARe-Gen adopts a query-point-based assembly representation. For each fragment, we adaptively sample sparse query points and perform query-driven tokenization to extract query-aligned local geometric tokens from a frozen shape encoder. Meanwhile, we jointly predict explicit contact structure during generation, including the localization of fractured-surface regions and a fragment-level adjacency graph. This turns adjacency from an implicit byproduct of the predicted assembly into a structural object that can be directly predicted and subsequently utilized to reason about inter-fragment relations. SARe-Refine then performs inference-time structure guided refinement. It verifies candidate adjacencies with geometric consistency checks and prunes unreliable edges to obtain a reliable sub-structure, then injects it as a stable constraint into a second inference pass to resample and correct the remaining uncertain regions, reducing error accumulation. Finally, we conduct systematic evaluations across three representative data settings, covering simulated fractures of synthetic objects, simulated fractures of scanned real-world objects, and scans of physically fractured objects. Experimental results show that SARe-Gen achieves state-of-the-art performance across all three settings, with particularly strong gains at large fragment counts. SARe-Refine further improves assembly quality by providing effective inference-time structural correction.

In summary, our key contributions are: (1) We identify explicit contact-structure modeling as the key to scalable reassembly, and propose **SARe-Gen** that jointly predicts contact graphs alongside pose generation. (2) We introduce **SARe-Refine**, a geometry-verified inference-time correction mechanism that anchors reliable substructures and resamples uncertain regions. (3) We build and release a large-scale fracture reassembly benchmark derived from real-world

scanned objects, providing $\sim 55\text{K}$ training samples with structural supervision signals (see Appendix for details). (4) Experiments across three data settings demonstrate state-of-the-art results with more graceful degradation at high fragment counts.

2 Related work

3D Fracture Reassembly. 3D fracture reassembly reconstructs an object by estimating each fragment’s rigid pose from randomly posed pieces. Unlike semantic part assembly, fracture fragments lack stable semantics and exhibit irregular fracture patterns [5, 19, 26, 57]. Thus, it hinges on fracture-surface geometric consistency and global inter-fragment compatibility.

Early unsupervised pipelines matched hand-crafted fracture features and solved assembly via global optimization [6, 10, 12, 46]. They work for small fractures, but degrade with ambiguity, mismatch accumulation, and combinatorial explosion as the number of fragments grows [2, 26]. Large-scale synthetic benchmarks have accelerated learning-based approaches. In particular, the Breaking Bad Dataset generates large-scale fragment data with diverse fracture patterns through physical simulation [36]. Recent methods learn cross-fragment interactions to regress relations and poses [33, 43]. Lu *et al.* propose Jigsaw to match and align fracture surfaces using hierarchical geometric features [27]. They further explore incorporating complete-shape priors to improve assembly stability [25]. More recent work adopts iterative denoising as a dominant paradigm. One line performs diffusion modeling in the pose parameter space and directly generates 6-DoF transformations by denoising. For instance, DiffAssemble combines diffusion models with graph neural networks [35]. PuzzleFusion++ uses a “denoise-and-verify” pipeline with a separately trained verifier [42]. GARF and RPF use flow-based denoising to align fragments, but both require extra pretrained conditioning heads [20, 39]. Building on these generative schemes, we also approach fracture assembly from a denoising-based perspective. However, instead of training an additional verifier or structural module beyond the main generator, we model inter-fragment adjacency as an explicit structural variable and make it directly usable at inference time.

3D Diffusion Model. Diffusion models have rapidly expanded from 2D image and video synthesis to 3D generation [52, 53]. Recent work commonly follows a two-stage paradigm: first, a 3D autoencoder learns a compact shape latent representation, and then diffusion or flow matching is performed in the latent space or a local token space [13, 45]. To efficiently represent 3D spatial structure in such latent spaces, a variety of structured latent designs have been explored; compared to explicit representations, implicit latents are typically more compact and enable smoother geometric modeling [29, 53]. One representative direction is structured sparse volumetric latents, exemplified by TRELLIS [45], with later extensions to watertight arbitrary-topology generation [22] and higher voxel resolutions [34]. Another direction represents shapes as a vecset latents:

3DShape2VecSet encodes a shape as a set of 1D latent vectors [53], and follow-up work improves this family with hierarchical latents [54] and improved 3D VAEs with systematic sampling [4]. Recent work [3, 55] further indicates the compositionality of tokenized latents: combining token subsets can be decoded, without retraining, into a good approximation of the union of the corresponding local geometries, supporting local token spaces as a scalable substrate for structural modeling. Inspired by this, we adopt Hunyuan3D-ShapeVAE [13] query-point-aligned local tokens as the implicit representation for fractured fragments, grounding tokens in Euclidean coordinates while encoding fine-grained fracture surface geometry.

Diffusion Models with External Representations. Introducing external representations into diffusion models, whether as intermediate semantic embeddings or as representation alignment objectives, has become an effective strategy for improving controllability, structural consistency and training stability. For example, Würstchen [32] learns highly compact semantic image representations to guide subsequent diffusion. RCG [21] generates semantic representations in a learned embedding space. REPA [51] aligns intermediate diffusion features with pretrained encoder representations. Another paradigm is that the external representation is not directly provided, but is jointly predicted by the model alongside the primary denoising objective. For instance, ShadowDiffusion [9] treats progressive shadow mask refinement as an auxiliary task. TopoDiffuser [48] introduces an auxiliary segmentation head optimized with pixel-wise loss jointly with the diffusion objective. Similarly, DiffusionMTL and TaskDiffusion [49, 50] incorporate multi-task dense prediction maps within a unified diffusion-denoising framework. Building upon this line of work, we jointly predict inter-fragment adjacency and fracture-surface tokens as auxiliary structural representations and optimize them together with the main denoising objective.

3 Reassembly Problem Formulation

Given a fractured object consisting of K fragments, we represent each fragment by a point set (or surface samples from a mesh) $\{\mathcal{P}_i\}_{i=1}^K$, where $\mathcal{P}_i = \{\mathbf{x}_{i,n} \in \mathbb{R}^3\}_{n=1}^{N_i}$ is defined in the local coordinate system of fragment i . The goal of 3D fragment reassembly is to recover a rigid transformation $\mathcal{T}_i = (R_i, \mathbf{t}_i) \in SE(3)$ for each fragment, where $R_i \in SO(3)$ and $\mathbf{t}_i \in \mathbb{R}^3$, so that the transformed fragment becomes

$$\mathcal{P}'_i = \mathcal{T}_i(\mathcal{P}_i) = \{R_i \mathbf{x} + \mathbf{t}_i \mid \mathbf{x} \in \mathcal{P}_i\}, \quad (1)$$

and the assembled shape is $\mathcal{X}' = \bigcup_{i=1}^K \mathcal{P}'_i$ in a common object coordinate system.

Previous works have pointed out that directly learning distributions on the $SE(3)$ manifold is not intuitive and may lead to unstable optimization [17, 56]. Moreover, pose variables lack local geometric semantics, and their validity strongly depends on the compatibility of fracture surfaces across fragments.

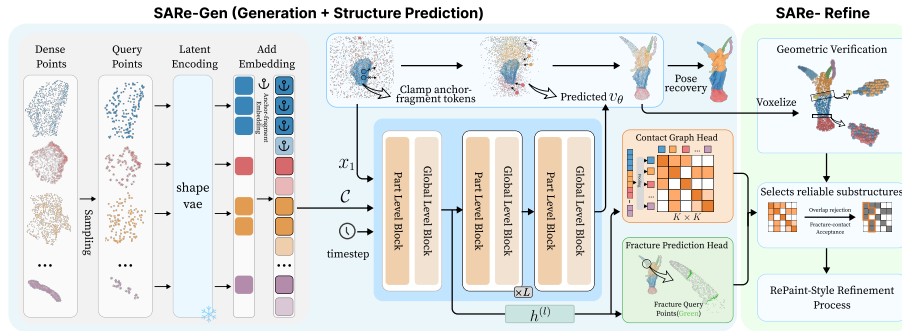


Fig. 2: Overview of SARE. SARE-Gen generates assembled query points in Euclidean space while predicting fracture-surface tokens and a contact graph. SARE-Refine optionally refines hard cases by keeping reliable substructures fixed and resampling uncertain regions.

To address these limitations, we reformulate the assembly problem at two complementary levels.

Inspired by [16, 39, 55], we formulate reassembly as conditional modeling in Euclidean space. Given the fragment set $\mathcal{P} = \{\mathcal{P}_i\}_{i=1}^K$ as the condition, we predict their assembled counterparts $\{\mathcal{P}'_i \subset \mathbb{R}^3\}_{i=1}^K$ in a shared global frame, whose union \mathcal{X}' represents a globally consistent assembly. Under rigid-body motion, each assembled fragment satisfies $\mathcal{P}'_i = \mathcal{T}_i(\mathcal{P}_i)$. Therefore, once $\{\mathcal{P}'_i\}$ are obtained, the rigid transforms $\{\mathcal{T}_i\}$ can be recovered by post-processing rigid alignment between \mathcal{P}_i and \mathcal{P}'_i .

A valid assembly is not merely a set of rigid transformations. It also induces contact structure among fragments, including which fragment pairs are in contact and where such contacts occur on fracture surfaces. We explicitly represent these two aspects with (i) an inter-fragment contact graph and (ii) fracture-surface point labels. We represent fragment-level contact relations with a symmetric adjacency matrix $A \in \{0, 1\}^{K \times K}$, where $A_{ij} = 1$ indicates that fragments i and j are in contact in the ground-truth assembly. For fragment i , we denote $F_i = \{f_i(\mathbf{x}) \in \{0, 1\} \mid \mathbf{x} \in \mathcal{P}_i\}$, where $f_i(\mathbf{x}) = 1$ indicates that \mathbf{x} lies on a contact fracture region.

In our framework, we predict assembled representations $\{\mathcal{P}'_i\}_{i=1}^K$ in Euclidean space and recover rigid transforms $\{\mathcal{T}_i\}$ via post-processing alignment, while jointly predicting contact structure A and $\{F_i\}$ to enable explicit reasoning and inference-time correction.

4 Method

We first introduce query-point conditioning to build query-aligned tokens, then present SARE-Gen for structure-aware generation, and finally describe SARE-Refine for inference-time refinement using predicted structure.

4.1 Query-Point Conditioning

To instantiate the conditional point-set generation in Sec. 3 with a scalable and point-aligned conditioning interface, we represent each fragment by a fixed-budget set of *query points* sampled from its dense point set. Concretely, for fragment i we first obtain a dense point set via importance sampling, and then select M_i query points using Farthest Point Sampling, yielding $\mathcal{Q}_i = \{q_{i,m}\}_{m=1}^{M_i}$ with $\mathcal{Q}_i \subset \mathcal{P}_i$ and enforce a per-object total budget $M = \sum_{i=1}^K M_i$, where M_i is allocated proportional to the fragment surface area. For each query point, we keep its input-frame coordinate and normal $(q_{i,m}^{in}, n_{i,m}^{in})$ and apply a positional encoding $\gamma(\cdot)$ [30, 40]. To capture local fracture geometry beyond sparse coordinates, we leverage a pretrained and frozen shape encoder ShapeVAE [13] to perform query-based tokenization. Specifically, for each query location, we extract a query-aligned local geometric token $z_{i,m}$ from fragment surface features. To disambiguate repetitive fragments, we inject the fragment identity via a part embedding e_i . Formally, the conditioning vector for the m -th query point of fragment i is

$$c_{i,m} = \phi([z_{i,m}; \gamma(q_{i,m}^{in}); \gamma(n_{i,m}^{in})]) + e_i, \quad (2)$$

where $\phi(\cdot)$ denotes a learnable linear projection. Aggregating all query points forms a set of point-aligned conditioning tokens $\mathcal{C} = \{c_{i,m}\}$, which will be used to condition the subsequent reassembly dynamics. Finally, following the common practice of using a reference fragment [20, 42], we select an anchor fragment (by the maximum M_i) and add a binary anchor embedding to its query-point tokens.

4.2 SARe-Gen: Structure-Aware Rectified Flow for Reassembly

Given the point-aligned conditioning tokens \mathcal{C} from the previous subsection, we model reassembly as conditional rectified flow to generate the assembled query points, while jointly predicting structural variables.

Rectified Flow. Following rectified flow with linear interpolation coupling and the conditional flow-matching objective [23, 24, 39], reassembly is modeled by learning a conditional velocity field in Euclidean space. Let the assembled query point set be $\mathcal{Q}' = \bigcup_{i=1}^K \mathcal{Q}'_i$, flattened as $x_0 \in \mathbb{R}^{M \times 3}$. A Gaussian endpoint $x_1 \sim \mathcal{N}(0, I)$ and a timestep $t \sim \mathcal{U}(0, 1]$ are sampled to define:

$$x_t = (1 - t)x_0 + tx_1, \quad v_t = \frac{dx_t}{dt} = x_1 - x_0. \quad (3)$$

The conditional velocity is parameterized as $v_\theta(x_t, t | \mathcal{C})$ and optimized via

$$\mathcal{L}_{\text{rf}} = \mathbb{E} \left[\left\| v_\theta(x_t, t | \mathcal{C}) - v_t \right\|_F^2 \right]. \quad (4)$$

In practice, v_θ is implemented as a DiT-style transformer operating on the M query points as tokens.

Joint structural prediction. To mitigate structural inconsistencies when K is large, two lightweight structural heads are attached to an intermediate

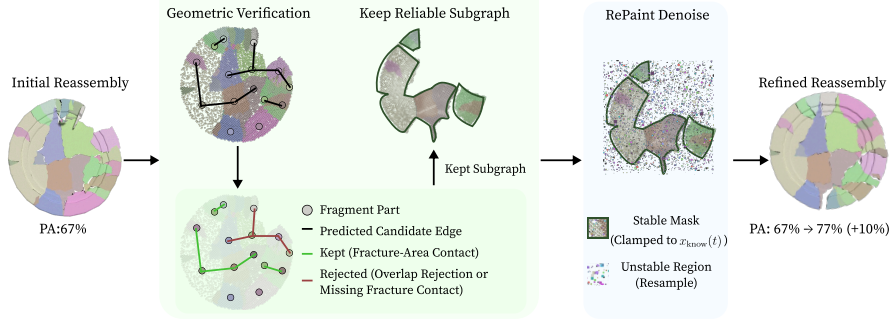


Fig. 3: SARE-Refine pipeline. Filter predicted edges, keep reliable substructures, then RePaint-style resample uncertain regions conditioned on a stable mask.

transformer token representation $h^{(\ell_s)} \in \mathbb{R}^{M \times D}$, where ℓ_s is the attachment layer index. Following representation supervision [51] and auxiliary multi-task diffusion [48–50], these auxiliary structural targets encourage noise-robust, structure-aware features. We predict token-level fracture-surface probabilities $\hat{f}_{i,m}$ with an MLP head, and predict the contact graph \mathcal{A} by pooling token features within each fragment to obtain part features and scoring part pairs. Both heads are trained with binary cross-entropy losses, denoted as \mathcal{L}_F and \mathcal{L}_A . Ground-truth labels for the fracture-surface token and the contact graph are obtained from dataset preprocessing.

Overall objective and anchor constraint. We jointly optimize

$$\mathcal{L} = \mathcal{L}_{\text{rf}} + \lambda_F \mathcal{L}_F + \lambda_A \mathcal{L}_A. \quad (5)$$

For the anchor fragment, we clamp the predicted velocity of anchor-fragment tokens to zero.

Pose recovery. We recover the rigid transform $\mathcal{T}_i = (R_i, \mathbf{t}_i)$ for each fragment by aligning its input-frame query points $\{q_{i,m}^{\text{in}}\}_{m=1}^{M_i}$ with the corresponding assembled query points $\{q'_{i,m}\}_{m=1}^{M_i}$.

4.3 SARE-Refine: Inference-Time Structure-Guided Refinement

SARE-Refine is an optional inference-time module that improves structural consistency for large- K assemblies. As illustrated in Fig. 3, it uses the structural predictions from SARE-Gen to identify reliable substructures, then anchors them as constraints during a second sampling pass to correct the remaining uncertain fragments.

We first run a complete inference pass to obtain an initial assembly $x^{(0)} \in \mathbb{R}^{M \times 3}$, along with token-level fracture probabilities $\hat{f}_{i,m}$ and a part-level adjacency score matrix \hat{A} from the structural heads. Directly thresholding \hat{A} often introduces spurious edges due to prediction noise, so we apply geometric verification to the candidate edge set E_{cand} derived from \hat{A} . For each candidate pair

$(i, j) \in E_{\text{cand}}$, we voxelize each fragment under its predicted pose to obtain the occupied voxel set S_i^v and map the predicted fracture tokens to the world frame to obtain fracture-region voxels F_i^v . Pairs whose fragments interpenetrate—measured by the voxel overlap ratio $r_{ij} = |S_i^v \cap S_j^v| / \min(|S_i^v|, |S_j^v|) > \tau_o$ —are discarded; among the rest, only pairs whose fracture regions sufficiently cover each other within a small voxel tolerance are retained. The verified edges E_{keep} induce a subgraph whose connected components above a minimum size form reliable substructures, with their token indices collected into a stable mask m_{st} .

In the second sampling pass, tokens in m_{st} are treated as a known region anchored to the first-pass positions x_{ref} . Under the straight-line coupling of rectified flow, the noise-consistent state for this region at timestep t is $x_{\text{known}}(t) = (1 - t)x_{\text{ref}} + t\epsilon$, where ϵ is the noise endpoint of the current trajectory. Inspired by RePaint-style inpainting [8, 28], we blend the stable region back before each model step via

$$x_t[m_{\text{st}}] \leftarrow (1 - \alpha)x_t[m_{\text{st}}] + \alpha x_{\text{known}}(t), \quad (6)$$

where $\alpha \in [0, 1]$ controls the injection strength, while keeping the anchor-fragment constraint from SARe-Gen unchanged. A resampling schedule repeatedly realigns the stable substructures throughout the trajectory. All hyperparameters are fixed and reported in the supplementary material.

5 Experiments

5.1 Experimental Setting

We use ShapeVAE [13] as a geometric encoder, and fix the total number of query points to $M = 5120$ per object. Our generator is a DiT-style transformer [31] with 12 blocks, following the architecture from RPF [39]. For structural prediction, we set $\ell_s = 4$ and attach lightweight structural heads to the intermediate hidden representation $h^{(\ell_s)}$ of the DiT backbone. We train the model for 100 epochs using AdamW with a learning rate of 1×10^{-4} , and set the loss weights to $\lambda_F = \lambda_A = 0.01$. All experiments are conducted on 4 NVIDIA RTX 4090 GPUs with a batch size of 8. In inference, we use Euler sampling with 50 steps. For SARe-Refine, we set the blending strength to $\alpha = 0.5$. Other implementation details are provided in the supplementary material.

Datasets. We evaluate our method on three datasets that cover synthetic fractures, simulated fractures from scanned real objects, and real-world physically fractured scans, with fragment counts ranging from $K = 2$ to 50. The vanilla Breaking Bad dataset [36] includes the *everyday* and *artifact* subsets, with a total of 55882 samples.⁵ We additionally preprocess the data to derive and cache structural supervision signals, including fracture-surface cues and the ground-truth adjacency matrix. From OmniObject3D [44], we select 1359 scanned objects and generate fractured data using the same pipeline as Breaking Bad [37], resulting

⁵ In the volume-constrained setting of Breaking Bad, the fragment count is capped at 33. In this work, we instead use the non-volume-constrained variant, which yields fragmented objects with K ranging from 2 to 50.

in 54966 samples, with an 80/20 split; detailed statistics and generation parameters are provided in the Appendix. We further evaluate on Fantastic Breaks [15], which contains 195 manually scanned fractured objects with complex surfaces.

Preprocessing and Augmentation. We center each object by its global centroid to define the object frame, and independently center each fragment to avoid leaking global pose information. During training, we keep the anchor fragment unrotated and apply random rigid rotations to the remaining fragments.

Evaluation Metrics. Following [20], we report the rotation error $\text{RMSE}(R)$ and the translation error $\text{RMSE}(T)$ as the root mean squared errors between the predicted and ground-truth fragment poses. We additionally report Part Accuracy (PA), defined as the fraction of correctly assembled fragments whose per-fragment Chamfer Distance to the ground truth is below a threshold (0.01 in our experiments). Finally, we report the object-level Chamfer Distance (CD) between the assembled shape and the ground-truth object.

Competing Methods. We compare against several fracture reassembly methods, including SE(3)-Equiv [43], DiffAssemble [35], Jigsaw [27], PuzzleFusion++ [42], GARF [20], and RPF [39]. For a fair large- K comparison under our $K \in [2, 50]$ setting, we reproduce GARF and RPF with an identical evaluation protocol. Specifically, for GARF, we modify the official implementation to extend its fragment-count support from at most 20 fragments to up to 50. For RPF, we re-train the official model on the vanilla Breaking Bad split under the same fragment-count range. For the remaining baselines, we report numbers from official papers or repositories, which are often reported under smaller- K settings (e.g., $K \leq 20$) and thus serve as reference results. For our SARE-Gen, we report results for two training setups: a model trained only on Breaking Bad and a model trained on joint data from all datasets.

5.2 Quantitative Evaluations

SARE-Gen Performance Evaluation. We first evaluate our SARE-Gen on the Breaking Bad benchmark (Table 1). SARE consistently improves assembly quality over prior methods in terms of part accuracy, object-level Chamfer distance, and pose errors, indicating that jointly modeling pose generation and explicit contact structure yields more reliable assemblies.

Meanwhile, we analyze the scalability of SARE as the fragment count increases. We partition the test set into several fragment-count bins and report the Part Accuracy (PA) aggregated within each bin (Fig. 1-a). The results show that SARE’s advantage becomes increasingly pronounced as K grows. This trend suggests that explicit contact-structure prediction acts as a strong inductive bias in high- K settings, improving global consistency when fragments are semantically ambiguous and contact patterns are dense. Since the compared baselines do not explicitly output adjacency relations, we induce a reference adjacency matrix from the predicted assemblies of GARF and RPF (Fig. 1-b). Concretely, for each fragment pair, we compute a proximity score (minimum inter-fragment surface distance) in the predicted assembly and threshold it to obtain an induced adjacency matrix (see supplementary for details). We then compare it

Table 1: Quantitative results on Breaking Bad (top), Fantastic Breaks and OmniObject3D (bottom).

Method	Everyday				Artifact			
	PA \uparrow %	CD \downarrow $\times 10^{-3}$	RMSE(R) \downarrow deg.	RMSE(T) \downarrow $\times 10^{-2}$	PA \uparrow %	CD \downarrow $\times 10^{-3}$	RMSE(R) \downarrow deg.	RMSE(T) \downarrow $\times 10^{-2}$
SE(3)-Equip	79.30	28.50	79.30	16.90	–	–	–	–
DiffAssemble	73.30	–	73.30	14.80	–	–	–	–
Jigsaw	57.30	13.30	42.30	10.70	45.60	14.30	52.40	22.20
PF++	70.60	6.03	38.10	8.04	49.60	14.50	52.10	13.90
GARF	81.46	1.28	21.04	4.57	80.05	2.16	20.81	5.10
RPF	83.07	0.96	22.35	4.06	84.92	1.06	27.57	4.62
SARe-Gen*	91.75	0.68	19.85	3.66	92.55	0.71	15.31	2.72
SARe-Gen	94.98	0.63	13.89	2.18	95.05	0.59	10.25	1.76

Method	Fantastic Breaks				OmniObject3D			
	PA \uparrow %	CD \downarrow $\times 10^{-3}$	RMSE(R) \downarrow deg.	RMSE(T) \downarrow $\times 10^{-2}$	PA \uparrow %	CD \downarrow $\times 10^{-3}$	RMSE(R) \downarrow deg.	RMSE(T) \downarrow $\times 10^{-2}$
GARF	91.00	2.12	10.62	2.10	80.12	1.32	22.54	5.37
RPF	87.30	2.53	16.69	2.18	82.32	1.35	20.06	4.33
SARe-Gen*	98.22	0.82	11.82	0.96	93.34	0.84	16.35	1.92
SARe-Gen	100.00	0.19	9.38	0.39	95.22	0.40	10.05	1.05

SARe-Gen* is trained on Breaking Bad only; SARe is trained with joint data from all datasets.

with the adjacency relations explicitly predicted by SARe. Although structure prediction becomes more challenging as the fragment count K increases, SARe still maintains relatively more stable adjacency quality.

We further evaluate cross-dataset generalization on Fantastic Breaks and OmniObject3D (Table 1), which differ from Breaking Bad in object categories, scanning noise, or fracture patterns. The results show that SARe remains competitive on these out-of-domain datasets, indicating that the learned structural cues are not tied to a specific data distribution and can transfer robustly across domains. Moreover, the jointly trained model further improves performance on both Fantastic Breaks and OmniObject3D, suggesting that increased geometric and structural diversity during training enhances robustness and generalization.

SARe-Refine Performance Evaluation. We observe that SARe-Refine brings little benefit when the first-pass SARe result is already highly accurate. Therefore, we apply SARe-Refine to all test samples and stratify them into bins according to the first-pass part accuracy (Table 2). We report the bin-wise improvements, and additionally summarize the average gain over samples with $PA_{\text{SARe}} \leq 95\%$ to better reflect its effect on harder cases. Aggregating the bins with first-pass $PA_{\text{SARe}} \leq 95\%$, this harder subset accounts for 24.98% (Everyday), 25.94% (Artifact), and 12.62% (OmniObject3D) of the test samples. On this subset, SARe-Refine consistently improves the mean PA from 79.75% to 82.24% (+2.49 pp, *i.e.*, percentage points) on Everyday, from 80.42% to 82.94% (+2.52 pp) on Artifact, and from 81.70% to 84.76% (+3.06 pp) on OmniObject3D. The bin-wise breakdown by the first-pass PA in Table 2 shows larger gains on more challenging inputs and diminishing improvements as the first-

Table 2: Effect of SARE-Refine on part accuracy. We report mean PA before/after refinement and Δ (pp) across PA bins, for the hard subset (first-pass PA $\leq 95\%$) and the full test set. Header percentages indicate the hard-subset ratio.

PA bin %	Everyday			Artifact			OmniObject3D		
	Gen PA %	Refine PA %	Δ pp	Gen PA %	Refine PA %	Δ pp	Gen PA %	Refine PA %	Δ pp
0-50	30.92	32.15	+1.23	36.99	38.64	+1.65	39.43	46.61	+7.18
50-60	52.51	57.95	+5.44	51.57	55.09	+3.52	53.75	57.12	+3.37
60-70	65.29	69.94	+4.65	66.41	71.15	+4.74	64.87	67.72	+2.85
70-80	75.27	79.24	+3.97	75.65	81.04	+5.39	75.07	79.58	+4.51
80-90	85.36	87.69	+2.33	85.35	87.74	+2.39	85.54	88.69	+3.15
90-95	92.78	93.55	+0.77	92.52	92.56	+0.04	92.50	93.96	+1.46
PA ≤ 95 subset	79.75	82.24	+2.49	80.42	82.94	+2.52	81.70	84.76	+3.06
Overall	94.98	95.60	+0.62	95.05	95.70	+0.65	95.22	96.23	+1.01

pass quality approaches 95%. Overall, averaging over the full test set also shows a consistent improvement with SARE-Refine.

5.3 Qualitative Evaluations.

Fig. 4 visualizes representative reassembly results of SARE, two baseline methods, and the ground truth, covering both easy cases with small fragment counts and challenging cases with large K . In small- K scenarios, other methods produce visually plausible assemblies and the differences are relatively minor. However, as K increases, the baselines tend to accumulate structural errors, such as incorrect fragment adjacencies and multiple contact conflicts, which eventually distort the global shape. We further include examples refined by SARE-Refine. In these cases, SARE-Refine improves the final assembly by verifying reliable substructures and performing conditional resampling on the remaining uncertain regions, correcting local structural mistakes while preserving already consistent parts. Finally, the last column shows several typical failure cases. They mostly occur when the object is fragmented into many thin, slice-like pieces, where distinctive geometric cues and stable contact regions are limited, making the assembly highly ambiguous and difficult for all methods.

5.4 Ablation Studies and Analyses

Table 3 presents an ablation study on the two structural prediction heads in SARE-Gen, including the fracture prediction head and the adjacency head. We further ablate the geometry encoder by replacing the frozen ShapeVAE with a frozen PTV3 point encoder while keeping the generator and training setup unchanged, using an RPF-style feature sampling to form input tokens. Removing both heads leads to a substantial drop in assembly performance, suggesting that relying solely on the generative backbone is insufficient for stable reassembly in challenging cases. Removing the fracture head degrades overall metrics, suggesting that fracture localization provides useful constraints for pose generation.

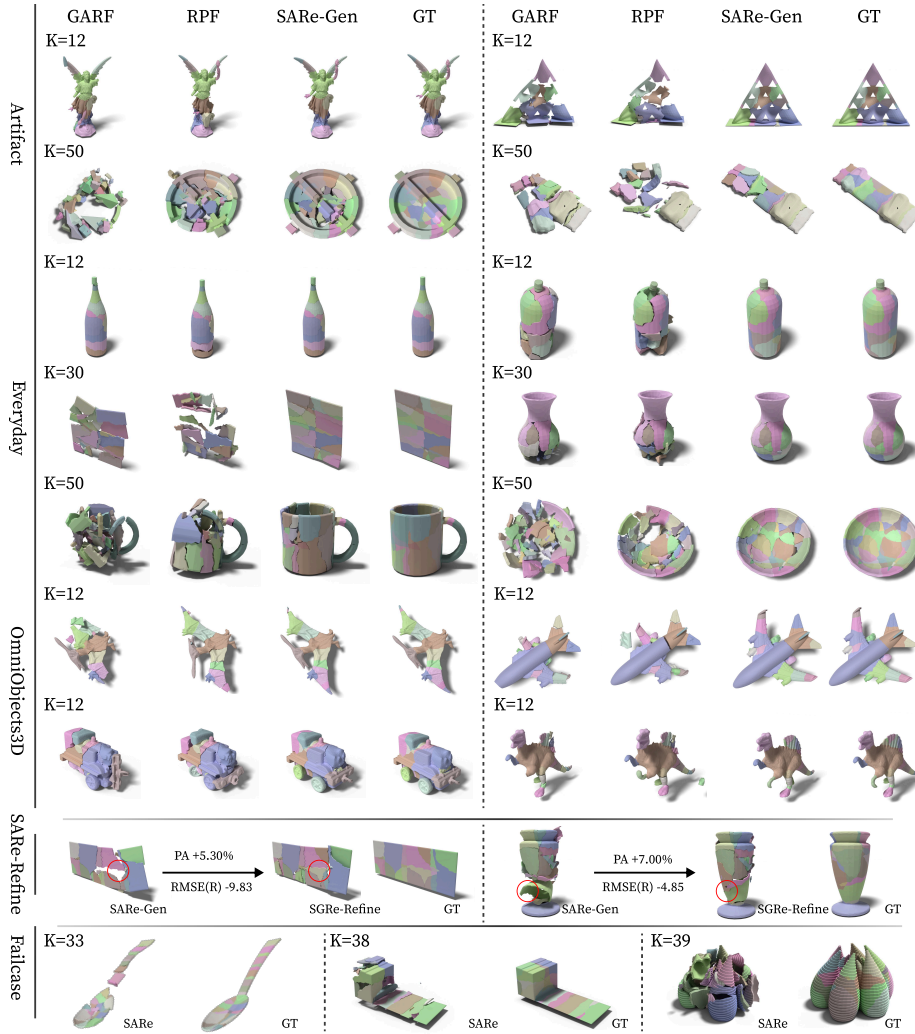


Fig. 4: Qualitative results of SARe-Gen and SARe-Refine, along with representative failure cases. (Please zoom in for a clearer view of the geometric details.)

Removing the adjacency head yields a larger drop in PA, highlighting the importance of explicit adjacency prediction for preserving correct inter-fragment relations. Table 4 further analyzes the effect of where to attach the structural heads (here we only use the Breaking Bad everyday subset). We attach the lightweight structural heads to different Transformer blocks and compare assembly quality and adjacency precision. The results suggest that attaching the heads at intermediate layers (4–6) achieves a better trade-off, maintaining high PA while yielding stronger adjacency precision. When the heads are attached too late (10–

Table 3: Ablation on SARE-Gen structural heads (fracture and adjacency), and geometry encoder.

	PA \uparrow %	CD \downarrow $\times 10^{-3}$	RMSE(R) \downarrow deg.	RMSE(T) \downarrow $\times 10^{-2}$	Frac. Prec. \uparrow %	Adj. Prec. \uparrow %
ShapeVAE \rightarrow PTv3	82.70	1.23	30.58	5.10	72.88	84.60
w/o-all head	87.36	0.95	26.58	4.00	–	–
w/o-fracture head	93.36	0.78	19.26	3.02	–	93.06
w/o-adj. head	88.52	0.95	22.86	3.55	78.01	–
Ours	95.00	0.61	12.71	2.04	78.74	93.79

Table 4: Effect of attachment layer on PA and adjacency precision.

Layer	PA (%) \uparrow	Adj. Prec. (%) \uparrow
2	87.95	80.98
4	92.75	92.94
6	92.77	91.33
8	91.70	86.44
10	88.95	74.04
12	87.17	74.24

Table 5: Ablation of SARE-Refine modes on Everyday.

Mode	PA (%) \uparrow	RMSE(R) \downarrow
Freeze	+0.11	-0.11
RePaint-0.5	+0.62	-0.53
RePaint-1.0	+0.52	-0.27

12), adjacency precision drops more noticeably, whereas PA changes only mildly. This trend indicates that deeper features are more specialized for pose generation, while intermediate representations are better suited for contact-structure prediction.

We ablate the refinement strategy on the Everyday subset by comparing a Freeze variant (keeping the stable region fixed without resampling) and RePaint-style second-pass resampling with different blending strengths α . Results are summarized in Table 5.

6 Conclusion

We present SARE, a structure-aware generative framework for large-scale 3D fragment reassembly that couples Euclidean-space assembly generation with explicit contact reasoning. SARE-Gen predicts assembled representations while jointly inferring fracture-surface cues and an inter-fragment contact graph, enabling contact structure to be used as actionable guidance rather than an implicit byproduct. Building on these predictions, SARE-Refine provides an inference-time correction mechanism that keeps reliable substructures fixed and resamples only uncertain regions, improving robustness when contact uncertainty accumulates. Extensive experiments across three data settings demonstrate state-of-the-art performance and more graceful degradation as the fragment count increases.

Although SARE-Gen performs global generation, errors can accumulate at very large K and cause structural drift. Future work will explore hierarchical autoregressive assembly with validated substructures and multimodal conditioning with texture and appearance cues to improve contact reasoning under partial and noisy observations.

References

1. Calzado-Martínez, A., García-Fernández, A.L., Ortega-Alvarado, L.M., Feito-Higueruela, F.R.: Integrated information system for 3d interactive reconstruction of an archaeological site. *J. Comput. Cult. Herit.* **16**(3) (2023). <https://doi.org/10.1145/3586077>
2. Castañeda, A.G., Brown, B., Rusinkiewicz, S., Funkhouser, T., Weyrich, T.: Global consistency in the automatic assembly of fragmented artefacts. In: *Proceedings of the 12th International Conference on Virtual Reality, Archaeology and Cultural Heritage*. p. 73–80. Eurographics Association (2011)
3. Chen, M., Wang, J., Shapovalov, R., Monnier, T., Jung, H., Wang, D., Ranjan, R., Laina, I., Vedaldi, A.: Autopartgen: Autoregressive 3d part generation and discovery. In: *NeurIPS (2025)*, <https://openreview.net/forum?id=1jJGBcpn7q>
4. Chen, R., Zhang, J., Liang, Y., Luo, G., Li, W., Liu, J., Li, X., Long, X., Feng, J., Tan, P.: Dora: Sampling and benchmarking for 3d shape variational auto-encoders. In: *CVPR*. pp. 16251–16261 (June 2025)
5. Chen, Y.C., Li, H., Turpin, D., Jacobson, A., Garg, A.: Neural shape mating: Self-supervised object assembly with adversarial shape priors. In: *CVPR*. pp. 12724–12733 (June 2022)
6. Funkhouser, T., Shin, H., Toler-Franklin, C., García Castañeda, A., Brown, B., Dobkin, D., Rusinkiewicz, S., Weyrich, T.: Learning how to match fresco fragments. *ACM Journal on Computing and Cultural Heritage* **4**(2) (2011). <https://doi.org/10.1145/2037820.2037824>
7. Ghasemipour, S.K.S., Kataoka, S., David, B., Freeman, D., Gu, S.S., Mordatch, I.: Blocks assemble! learning to assemble with large-scale structured reinforcement learning. In: Chaudhuri, K., Jegelka, S., Song, L., Szepesvari, C., Niu, G., Sabato, S. (eds.) *Proceedings of the 39th International Conference on Machine Learning. Proceedings of Machine Learning Research*, vol. 162, pp. 7435–7469. PMLR (2022)
8. Go, H., Park, B., Jang, J., Kim, J.Y., Kwon, S., Kim, C.: Splatflow: Multi-view rectified flow model for 3d gaussian splatting synthesis. In: *CVPR*. pp. 21524–21536 (June 2025)
9. Guo, L., Wang, C., Yang, W., Huang, S., Wang, Y., Pfister, H., Wen, B.: Shadowdiffusion: When degradation prior meets diffusion model for shadow removal. In: *CVPR*. pp. 14049–14058 (2023)
10. Hong, J.H., Yoo, S.J., Zeeshan, M.A., Kim, Y.M., Kim, J.: Structure-from-sherds: Incremental 3d reassembly of axially symmetric pots from unordered and mixed fragment collections. In: *ICCV*. pp. 5423–5431 (2021). <https://doi.org/10.1109/ICCV48922.2021.00539>
11. Huang, J., Zhan, G., Fan, Q., Mo, K., Shao, L., Chen, B., Guibas, L., Dong, H.: Generative 3d part assembly via dynamic graph learning. In: *NeurIPS (2020)*
12. Huang, Q.X., Flöry, S., Gelfand, N., Hofer, M., Pottmann, H.: Reassembling fractured objects by geometric matching. *ACM TOG* **25**(3), 569–578 (2006). <https://doi.org/10.1145/1141911.1141925>
13. Hunyuan3d: Hunyuan3d 2.0: Scaling diffusion models for high resolution textured 3d assets generation (2025), [arXiv:2501.12202](https://arxiv.org/abs/2501.12202)
14. Jia, C., Ren, Y., Wang, Z., Zhang, Y.: Geoassemble: A geometry-aware hierarchical method for point cloud-based multi-fragment assembly. *Sensors* **25**(21) (2025). <https://doi.org/10.3390/s25216533>, <https://www.mdpi.com/1424-8220/25/21/6533>

15. Lamb, N., Palmer, C., Molloy, B., Banerjee, S., Banerjee, N.K.: Fantastic breaks: A dataset of paired 3d scans of real-world broken objects and their complete counterparts. In: CVPR. pp. 4681–4691 (2023). <https://doi.org/10.1109/CVPR52729.2023.00454>
16. Lan, Y., Zhou, S., Lyu, Z., Hong, F., Yang, S., Dai, B., Pan, X., Loy, C.C.: Gaussiananything: Interactive point cloud latent diffusion for 3d generation. In: ICLR (2025)
17. Leach, A., Schmon, S.M., Degiacomi, M.T., Willcocks, C.G.: Denoising diffusion probabilistic models on $SO(3)$ for rotational alignment. In: ICLR 2022 Workshop on Geometrical and Topological Representation Learning (GTRL) (2022), <https://openreview.net/forum?id=BY88eBbkpe5>
18. Lee, N., Min, J., Lee, J., Kim, S., Lee, K., Park, J., Cho, M.: 3D geometric shape assembly via efficient point cloud matching. In: Proceedings of the 41st International Conference on Machine Learning. Proceedings of Machine Learning Research, vol. 235, pp. 26856–26873. PMLR (21–27 Jul 2024)
19. Li, J., Cheng, C., Ma, J., Liu, G.: Geometric point attention transformer for 3d shape reassembly (2024), arXiv:2411.17788
20. Li, S., Jiang, Z., Chen, G., Xu, C., Tan, S., Wang, X., Fang, I., Zyskowski, K., McPherron, S.P., Iovita, R., Feng, C., Zhang, J.: Garf: Learning generalizable 3d reassembly for real-world fractures. In: ICCV. pp. 5711–5721 (October 2025)
21. Li, T., Katabi, D., He, K.: Return of unconditional generation: A self-supervised representation generation method. In: NeurIPS. vol. 37, pp. 125441–125468. Curran Associates, Inc. (2024). <https://doi.org/10.52202/079017-3985>
22. Li, Z., Wang, Y., Zheng, H., Luo, Y., Wen, B.: Sparc3d: Sparse representation and construction for high-resolution 3d shapes modeling. In: NeurIPS (2025)
23. Liu, Q.: Rectified flow: A marginal preserving approach to optimal transport (2022), arXiv:2209.14577
24. Liu, X., Gong, C., Liu, Q.: Flow straight and fast: Learning to generate and transfer data with rectified flow. In: ICLR (2023), <https://openreview.net/forum?id=XVjTT1nw5z>
25. Lu, J., Hua, G., Huang, Q.: Jigsaw++: Imagining complete shape priors for object reassembly. In: ICCV. pp. 6704–6714 (October 2025)
26. Lu, J., Liang, Y., Han, H., Hua, J., Jiang, J., Li, X., Huang, Q.X.: A survey on computational solutions for reconstructing complete objects by reassembling their fractured parts. *Computer Graphics Forum* **44** (2024)
27. Lu, J., Sun, Y., Huang, Q.: Jigsaw: Learning to assemble multiple fractured objects. In: NeurIPS. vol. 36, pp. 14969–14986. Curran Associates, Inc. (2023)
28. Lugmayr, A., Danelljan, M., Romero, A., Yu, F., Timofte, R., Van Gool, L.: Repaint: Inpainting using denoising diffusion probabilistic models. In: CVPR. pp. 11461–11471 (June 2022)
29. Mescheder, L., Oechsle, M., Niemeyer, M., Nowozin, S., Geiger, A.: Occupancy networks: Learning 3d reconstruction in function space. In: CVPR (2019)
30. Mildenhall, B., Srinivasan, P.P., Tancik, M., Barron, J.T., Ramamoorthi, R., Ng, R.: Nerf: Representing scenes as neural radiance fields for view synthesis. In: ECCV. Springer International Publishing (2020). https://doi.org/10.1007/978-3-030-58452-8_24, https://doi.org/10.1007/978-3-030-58452-8_24
31. Peebles, W., Xie, S.: Scalable diffusion models with transformers. arXiv preprint arXiv:2212.09748 (2022)
32. Perniás, P., Rampas, D., Richter, M.L., Pal, C.J., Aubreville, M.: Würstchen: An efficient architecture for large-scale text-to-image diffusion models. In: International

- Conference on Learning Representations (ICLR) (2024), [<https://openreview.net/forum?id=gU58d5QeGv>] (<https://openreview.net/forum?id=gU58d5QeGv>)
33. Qin, Z., Yu, H., Wang, C., Guo, Y., Peng, Y., Xu, K.: Geometric transformer for fast and robust point cloud registration. In: CVPR. pp. 11133–11142 (2022). <https://doi.org/10.1109/CVPR52688.2022.01086>
 34. Ren, X., Huang, J., Zeng, X., Museth, K., Fidler, S., Williams, F.: Xcube: Large-scale 3d generative modeling using sparse voxel hierarchies. In: CVPR. pp. 4209–4219 (2024). <https://doi.org/10.1109/CVPR52733.2024.00403>
 35. Scarpellini, G., Fiorini, S., Giuliari, F., Morerio, P., Del Bue, A.: Diffassemble: A unified graph-diffusion model for 2d and 3d reassembly. In: CVPR (June 2024)
 36. Sellán, S., Chen, Y.C., Wu, Z., Garg, A., Jacobson, A.: Breaking bad: A dataset for geometric fracture and reassembly. In: NeurIPS. vol. 35, pp. 38885–38898 (2022)
 37. Sellán, S., Luong, J., Mattos Da Silva, L., Ramakrishnan, A., Yang, Y., Jacobson, A.: Breaking good: Fracture modes for realtime destruction. ACM TOG **42**(1) (2023). <https://doi.org/10.1145/3549540>, <https://doi.org/10.1145/3549540>
 38. Shen, Y., Wu, R., Ke, Y., Song, X., Li, Z., Li, X., Fan, H., Lu, H., Dong, H.: Biassemble: Learning collaborative affordance for bimanual geometric assembly. In: ICML (2025)
 39. Sun, T., Zhu, L., Huang, S., Song, S., Armeni, I.: Rectified point flow: Generic point cloud pose estimation. In: NeurIPS (2025)
 40. Tancik, M., Srinivasan, P.P., Mildenhall, B., Fridovich-Keil, S., Raghavan, N., Singhal, U., Ramamoorthi, R., Barron, J.T., Ng, R.: Fourier features let networks learn high frequency functions in low dimensional domains. In: NeurIPS. vol. 33 (2020)
 41. Tselmelis, T., Palmieri, L., Khoroshiltseva, M., Islam, A., Elkin, G., Shahar, O.I., Scarpellini, G., Fiorini, S., Ohayon, Y., Alali, N., Aslan, S., Morerio, P., Vascon, S., Gravina, E., Napolitano, M.C., Scarpati, G., Zuchriegel, G., Spühler, A., Fuchs, M.E., James, S., Ben-Shahar, O., Pelillo, M., Del Bue, A.: Re-assembling the past: The repair dataset and benchmark for real world 2d and 3d puzzle solving. In: Globerson, A., Mackey, L., Belgrave, D., Fan, A., Paquet, U., Tomczak, J., Zhang, C. (eds.) NeurIPS. vol. 37, pp. 30076–30105 (2024). <https://doi.org/10.52202/079017-0947>
 42. Wang, Z., Chen, J., Furukawa, Y.: Puzzlefusion++: Auto-agglomerative 3d fracture assembly by denoise and verify. In: ICLR (2025)
 43. Wu, R., Tie, C., Du, Y., Zhao, Y., Dong, H.: Leveraging se(3) equivariance for learning 3d geometric shape assembly. In: ICCV. pp. 14265–14274 (2023). <https://doi.org/10.1109/ICCV51070.2023.01316>
 44. Wu, T., Zhang, J., Fu, X., Wang, Y., Ren, J., Pan, L., Wu, W., Yang, L., Wang, J., Qian, C., Lin, D., Liu, Z.: Omniobject3d: Large-vocabulary 3d object dataset for realistic perception, reconstruction and generation. In: CVPR. pp. 803–814 (2023). <https://doi.org/10.1109/CVPR52729.2023.00084>
 45. Xiang, J., Lv, Z., Xu, S., Deng, Y., Wang, R., Zhang, B., Chen, D., Tong, X., Yang, J.: Structured 3d latents for scalable and versatile 3d generation. In: CVPR. pp. 21469–21480 (June 2025)
 46. Xu, J., Zhou, M., Wu, Z., Shui, W., Ali, S.: Robust surface segmentation and edge feature lines extraction from fractured fragments of relics. *Journal of Computational Design and Engineering* **2**(2), 79–87 (2015). <https://doi.org/https://doi.org/10.1016/j.jcde.2014.12.002>
 47. Xu, Q.C., Chen, H.X., Hua, J., Zhan, X., Yang, Y.L., Mu, T.J.: Fragmentdiff: A diffusion model for fractured object assembly. In: SIGGRAPH Asia 2024 Conference Papers. Association for Computing Machinery, New York, NY, USA (2024). <https://doi.org/10.1145/3680528.3687673>

48. Xu, Z., Wang, J., Shi, Y., Gao, C., Zhou, G.: Topodiffuser: A diffusion-based multi-modal trajectory prediction model with topometric maps (2025), arXiv:2508.00303
49. Yang, Y., Jiang, P.T., Hou, Q., Zhang, H., Chen, J., Li, B.: Multi-task dense predictions via unleashing the power of diffusion. In: ICLR (2025)
50. Ye, H., Xu, D.: Diffusionmtl: Learning multi-task denoising diffusion model from partially annotated data. In: CVPR (2024)
51. Yu, S., Kwak, S., Jang, H., Jeong, J., Huang, J., Shin, J., Xie, S.: Representation alignment for generation: Training diffusion transformers is easier than you think. In: ICLR (2025), [<https://openreview.net/forum?id=DJSZGGZYVi>] (<https://openreview.net/forum?id=DJSZGGZYVi>)
52. zeng, x., Vahdat, A., Williams, F., Gojcic, Z., Litany, O., Fidler, S., Kreis, K.: Lion: Latent point diffusion models for 3d shape generation. In: Koyejo, S., Mohamed, S., Agarwal, A., Belgrave, D., Cho, K., Oh, A. (eds.) NeurIPS. vol. 35, pp. 10021–10039. Curran Associates, Inc. (2022), https://proceedings.neurips.cc/paper_files/paper/2022/file/40e56dabe12095a5fc44a6e4c3835948-Paper-Conference.pdf
53. Zhang, B., Tang, J., Nießner, M., Wonka, P.: 3dshape2vecset: A 3d shape representation for neural fields and generative diffusion models. ACM TOG **42**(4) (2023). <https://doi.org/10.1145/3592442>
54. Zhang, B., Wonka, P.: LaGeM: A large geometry model for 3d representation learning and diffusion. In: ICLR (2025), <https://openreview.net/forum?id=720S038a2z>
55. Zhao, W., Cao, Y.P., Xu, J., Dong, Y., Shan, Y.: Assembler: Scalable 3d part assembly via anchor point diffusion. In: Proceedings of the SIGGRAPH Asia 2025 Conference Papers. SA Conference Papers '25, Association for Computing Machinery (2025). <https://doi.org/10.1145/3757377.3763972>
56. Zhou, Y., Barnes, C., Lu, J., Yang, J., Li, H.: On the continuity of rotation representations in neural networks. In: CVPR. pp. 5738–5746 (2019). <https://doi.org/10.1109/CVPR.2019.00589>
57. Zuchtriegel, G., Brunetto, M.A., Gravina, E., Napolitano, M.C., Ricciardi, F.S., Zambrano, A., Khoroshiltseva, M., Palmieri, L., Pelillo, M., Vascon, S., Elkin, G., Shahar, O.I., Ohayon, Y., Alali, N., Ben-Shahar, O.: The repair project: Datasets for archaeological and restoration studies in pompeii. In: Digital Heritage. The Eurographics Association (2025). <https://doi.org/10.2312/dh.20253389>